Supplementary Information

Spatially Resolved Optoelectronic Puddles of WTe_2-2D Te Heterostructure

Thi Uyen Tran,[a,‡] Ngoc Thanh Duong,[b,‡] Daeyoung Park,[c] Jaeuk Bahng,[a] Hai Phuong Duong,[b] Van Dam Do,[d] Mun Seok Jeong,[c] and Seong Chu Lim[*,a,b]*

[a] *Department of Smart Fab. Technology, Sungkyunkwan University (SKKU), Suwon 16419, Republic of Korea.*

[b] *Department of Energy Science, Sungkyunkwan University (SKKU), Suwon 16419, Republic of Korea.*

[c] *Department of Physics, and Department of Energy Engineering, Hanyang University, Seoul 04763, Republic of Korea.*

[d] *Department of Electrical and Computer Engineering, Sungkyunkwan University (SKKU), Suwon 16419, Republic of Korea.*

‡ T.U.T. and N. T. D. contributed equally to this work.

** E-mail: seonglim@skku.edu*

1. X-ray diffraction (XRD) measurement of 2D Te and WTe_2.

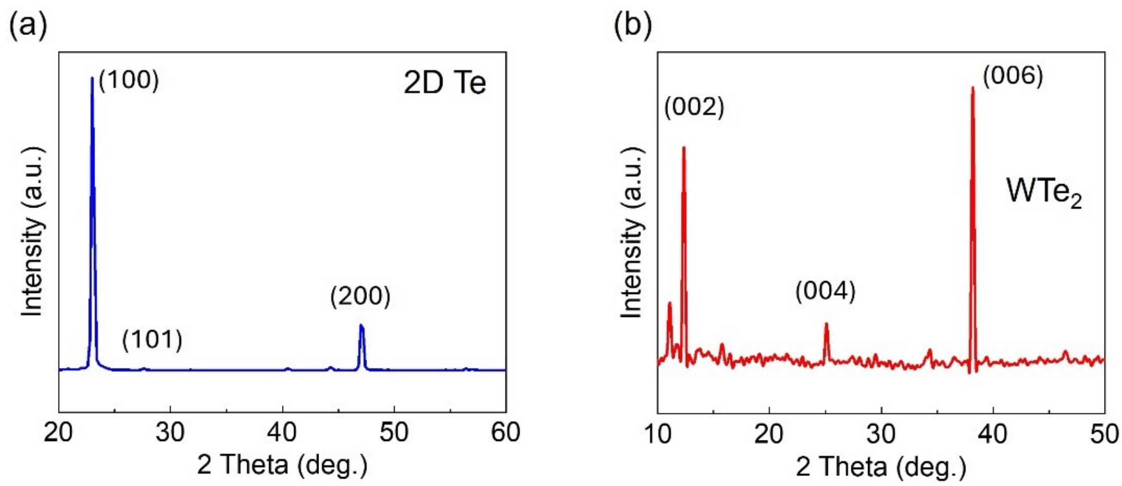

Figure S1. X-ray Diffraction spectrum of (a) 2D Te and (b) WTe_2

The crystalline sizes of 2D Te and WTe_2 were calculated via Scherrer's equation:

$$D = \frac{K\lambda}{\beta \cos\theta}$$

D, K λ, β are the size of grain (thickness of flake), Scherrer constant (0.9), wavelength of x-ray (Cu Kα = 0.154 nm), and FHWM value of diffraction peak, respectively.

In the XRD result, the (002) peak of WTe_2 is observed at 12.3584° with an FWHM value of 0.24482°. Applying the Scherrer equation to the result, the average value of crystalline size (D) of mechanically exfoliated WTe_2 flake is calculated as 32.6 nm.

Given the 2D Te (100) peak diffraction at 23.05179° with FWHM of 0.27206°, the calculated D value is 29.44 nm.

2. Atomic force microscopy (AFM) measurement

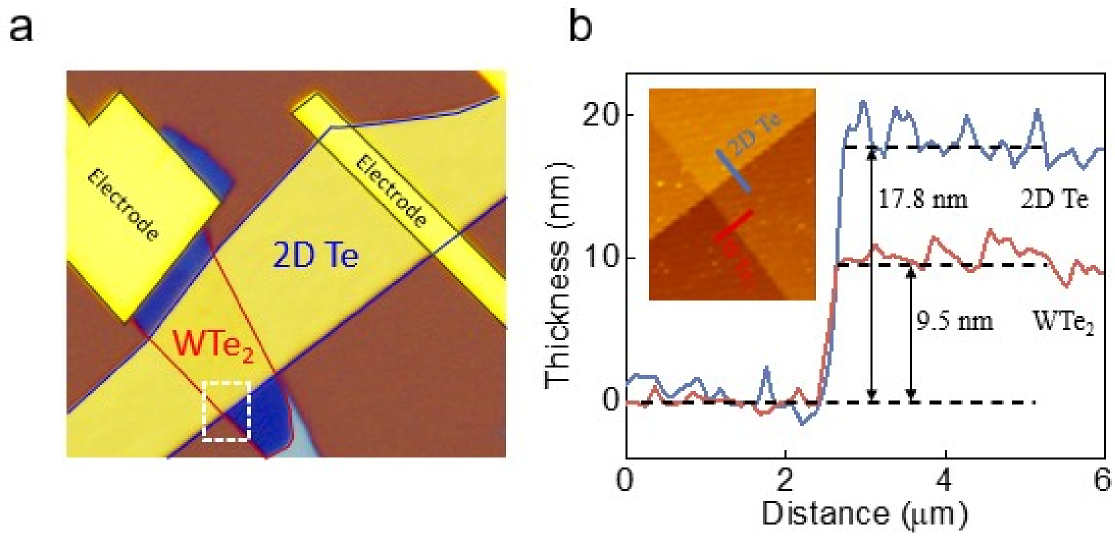

Figure S2. (a) Optical image of the WTe_2-2D Te heterostructure. (b) The inset shows an AFM topography image of the scanning area, which is marked by a white dashed line. The individual thickness profiles of the WTe_2 and 2D Te flakes were extracted across the red and blue lines, respectively.

3. Raman mapping of WTe_2 and 2D Te

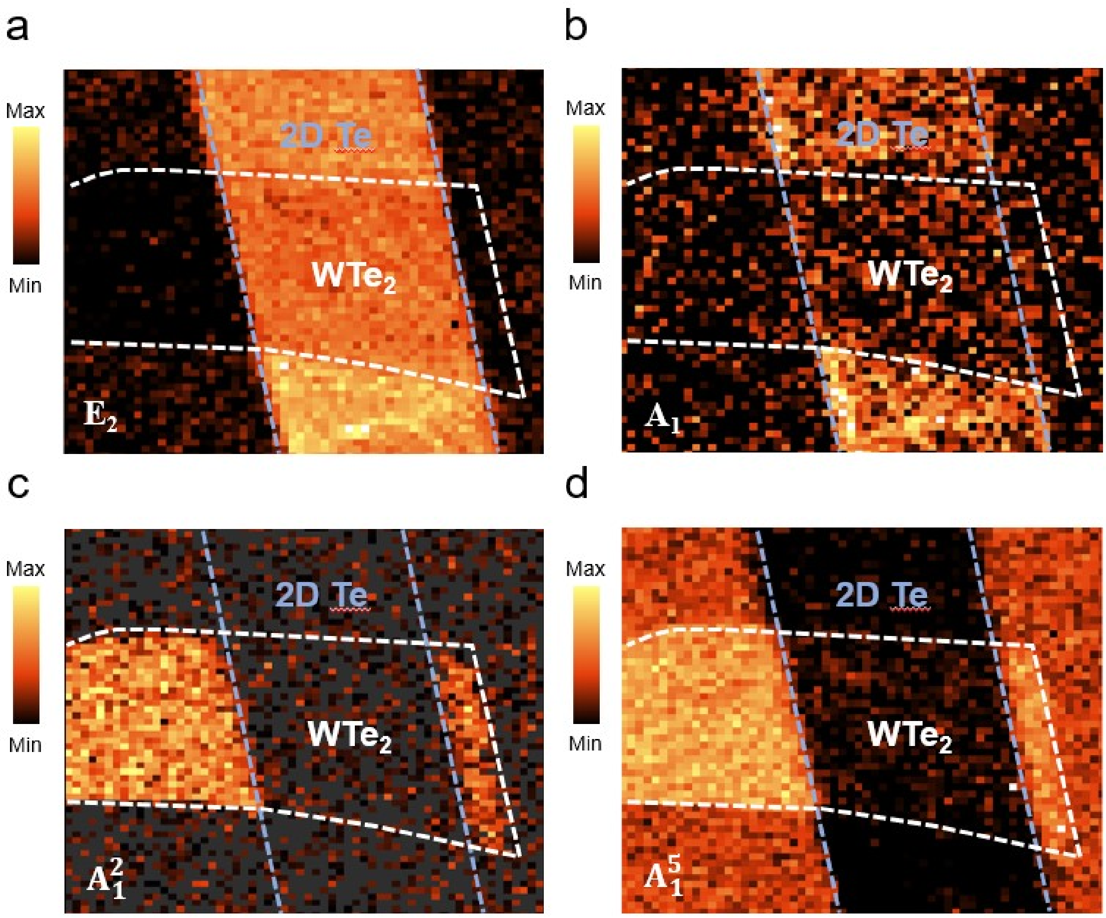

Figure S3. Raman mapping of the (a) E_2 and (b) A_1 vibration modes in WTe_2. Raman mapping of (c) A_1^2 and (d) A_1^5 vibration modes in 2D Te.

4. 2D Te and WTe_2 field effect transistors

The transfer curves of two distinct devices utilizing varying thicknesses of 2D Te were shown in Figures S4a and S4b. It is observed that the device with a thinner 2D Te (S4a) exhibits a notable reduction in current compared to devices with thicker channels (S4b). This suggests potential limitations in electronic and thermal performance within our heterostructure. Therefore, a relatively thick 2D Te (~ 18 nm) was proposed for use in the heterostructure.

Individual 2D Te and WTe_2 devices displayed linear behavior in their output characteristics, as shown in Figures S4c and S4d, suggesting that ohmic contacts were well established in both devices. The drain current (I_{ds}) of 2D Te was reduced at high V_{gs}, implying a p-type behavior of 2D Te. The I_{ds} of WTe_2 remained unchanged with V_{gs} because of its semi-metallic behavior.

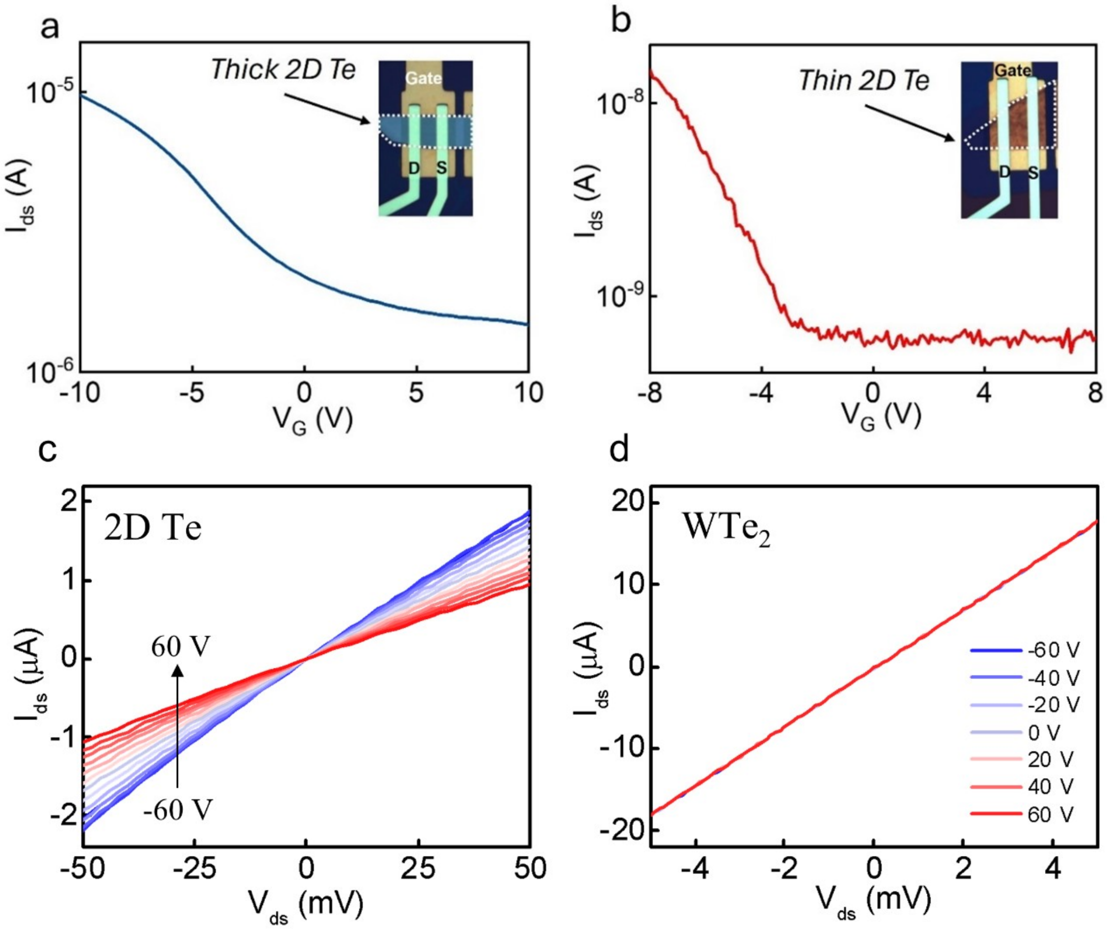

Figure S4. Transfer characteristics of 2D Te devices with (a) thinner and (b) thicker flakes. Output characteristics of the (c) 2D Te and (d) WTe_2 devices.

5. AC photocurrent mapping system

The magnitude-, phase-, and position-resolved photocurrents were measured using a self-designed a.c. photocurrent photocurrent-mapping system, as illustrated in Figure S4a. A laser source with a wavelength of 532 nm was tightly focused into a spot with a 1-µm diameter through a numerical aperture (NA = 0.6) objective lens. V_{ds} and V_{gs} were applied using a pre-amplifier (SR570) and a dual-channel source meter (2636 B), respectively. When the focused laser beam scanned the sample, a laser-induced current was obtained and amplified using a pre-amplifier (SR570). The magnitude and phase of AC photocurrent were measured using a lock-in amplifier synchronized with an optical chopper, as shown in Figure S10b.

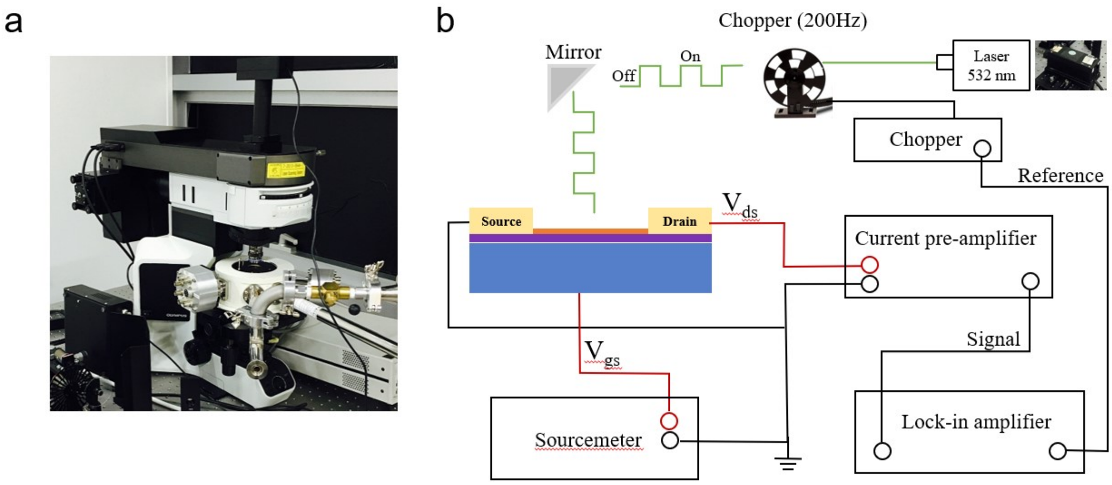

Figure S5. Photograph (a) and schematic circuitry (b) for the self-designing AC photocurrent mapping system.

6. Kelvin Probe Force Microscopy (KPFM) measurement of WTe-2D Te, heterojunction

To clarify the photovoltaic (PV) effect at the junction of WTe_2 and 2D Te, we performed Kelvin Probe Force Microscopy (KPFM). Through KPFM measurements, we estimated the work functions of WTe_2, 2D Te, and their heterojunction to be 4.32 eV, 4.65 eV, and 4.5 eV, respectively. As a result, an accumulation mode was formed at the junction, playing an important role in photocarrier separation of PV.

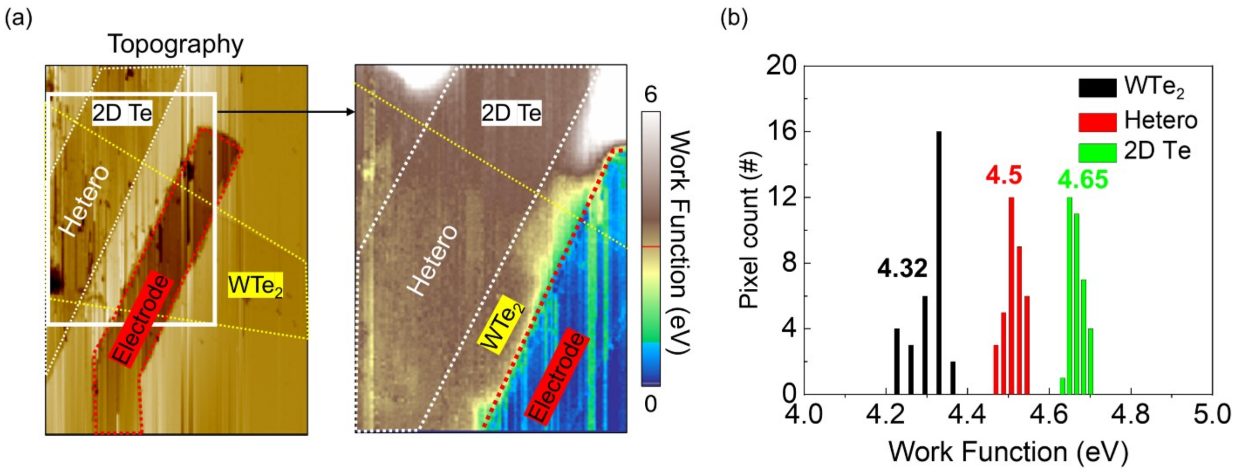

Figure S6. (a) KPFM surface potential and (b) work function distributions of WTe_2, 2D Te, and their heterojunction.

7. Photocurrent map from WTe_2-2D Te at V_{ds} = 0 V as a function of V_{gs}

The modulations of the photocurrent intensity, direction, and position in the WTe_2-2D Te heterojunction were registered as a function of V_{gs} using our system. As shown in Figure S5, the backgate bias was swept from V_{gs} = -40 V to V_{gs} = 40 V at V_{ds} = 0 V. The photothermoelectric current at the heterojunction, which arose from the thermal voltage difference between 2D Te and WTe_2 layers, dominated the photocurrent mechanism at V_{ds} = 0 V, particularly at higher V_{gs} values.

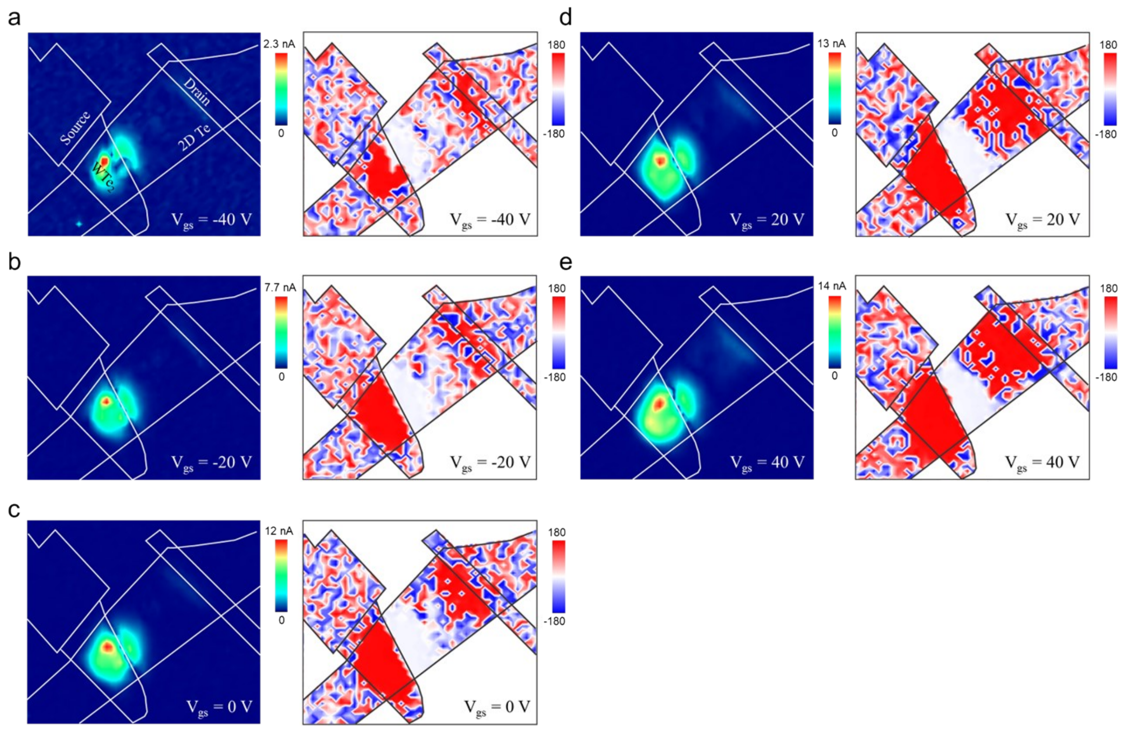

Figure S7. Magnitude-, phase-, and position-resolved photocurrent maps of WTe_2-2D Te as a function of V_{gs} at V_{ds} = 0 V. The input optical power is 5 μW. (a) V_{gs} = -40 V, (b) V_{gs} = -20 V, (c) V_{gs} = 0 V, (d) V_{gs} = 20 V, and (e) V_{gs} = 40 V.

8. Seebeck coefficient measurement of 2D Te and WTe_2 devices

A temperature gradient across the sample was created by applying a DC current of 10 mA to the serpentine electrode to estimate the Seebeck coefficients of 2D Te and WTe_2. These electrodes were patterned using electron beam lithography, followed by Cr/Au (10/100 nm) deposition (Figures S6a and 6d). The local resistances of the top and bottom electrodes of 2D Te and WTe_2 were measured using two 4-terminal electrodes. The top and bottom electrode temperatures of 2D Te and WTe_2 are estimated using the pre-calibrated resistance-temperature relationship shown in Figures S6b and S6d, respectively. The voltage induced by the temperature gradient was measured using a Keithley 2182A Nanovoltmeter. The Seebeck coefficients of 2D Te and WTe_2 were measured at 300 K by adjusting V_{gs}. The measurement of thermoelectric power was carried out inside a closed cycle refrigerator (CCR) with a base pressure of 5×10^{-6} torr.

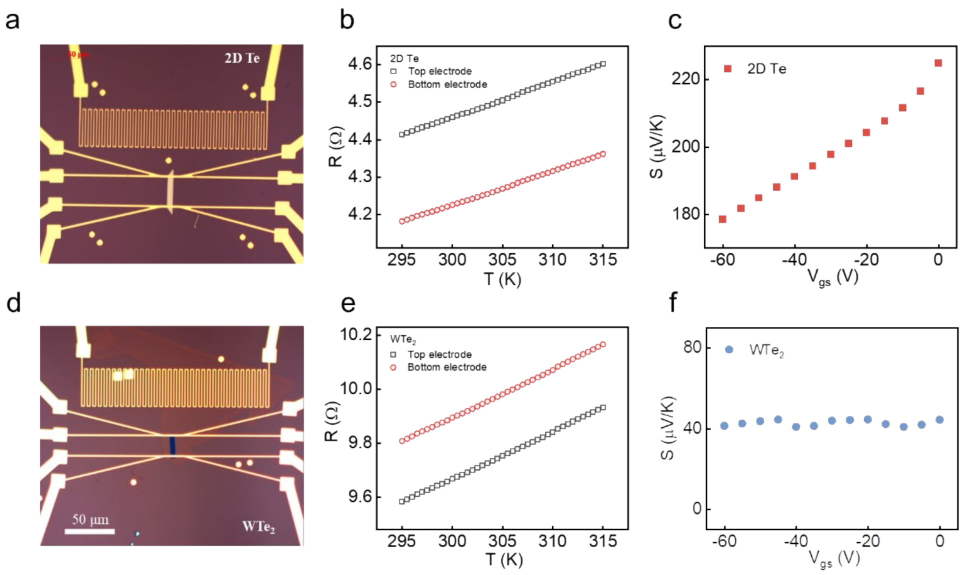

Figure S8. (a) 2D Te and (d) WTe_2 device structures for thermoelectric power measurement. Temperature-resistance relations of top and bottom electrodes in (b) 2D Te and (e) WTe_2 devices. Seebeck coefficients versus gate voltage of (c) 2D Te and (d) WTe_2.

9. Power dependent photocurrent

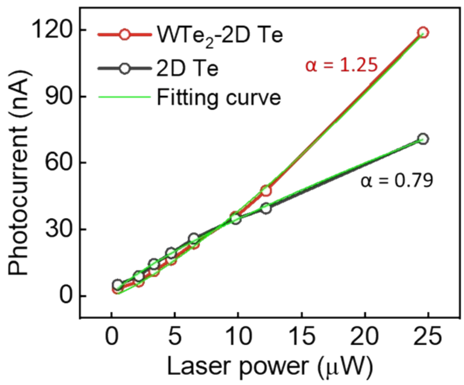

Figure S9. Power dependent photothermoelectric current of 2D Te in region (1) and WTe_2-2D Te heterojunction in region (3).

10. Photocurrent mapping of 2D Te and WTe_2 devices using NIR

The detection range and sensitivity of photodetectors depend on the wavelength of incident light. We scrutinized the PTE behavior of our heterostructure using near-infrared (NIR) 1064 nm and compared these findings with those obtained at 532 nm. It is noted that the wavelength 1064 nm is visible to the Si image sensor built into our photocurrent mapping systems to gain the mapping images. Under V_{ds} = 0 V and V_{gs} = 0 V, as shown in Figure S9, the PTE effect thrives much more with 1064 nm compared to the device shined at 532 nm in Figure S7c. Despite the same incident powers, 5 μW, were illuminated on devices, the photothermal current ranges about 12nA at the maximum in Fig. S7c. However, when the junction was excited by 1064 nm, we gained a photothermal current of approximately 44 nA at its peak. Our findings are consistent with those of a previous study [1]. We attribute the enhanced PTE of our heterostructure to WTe_2. Under zero bias across the entire heterojunction, altering the wavelength of incident light from 532 nm to 1064 nm significantly impacts the absorption properties of WTe_2, in contrast to 2D Te. This is expected because the free carrier absorption, α, of semimetal WTe_2 promotes longer wavelength, $\alpha \sim \lambda^2$ [2].

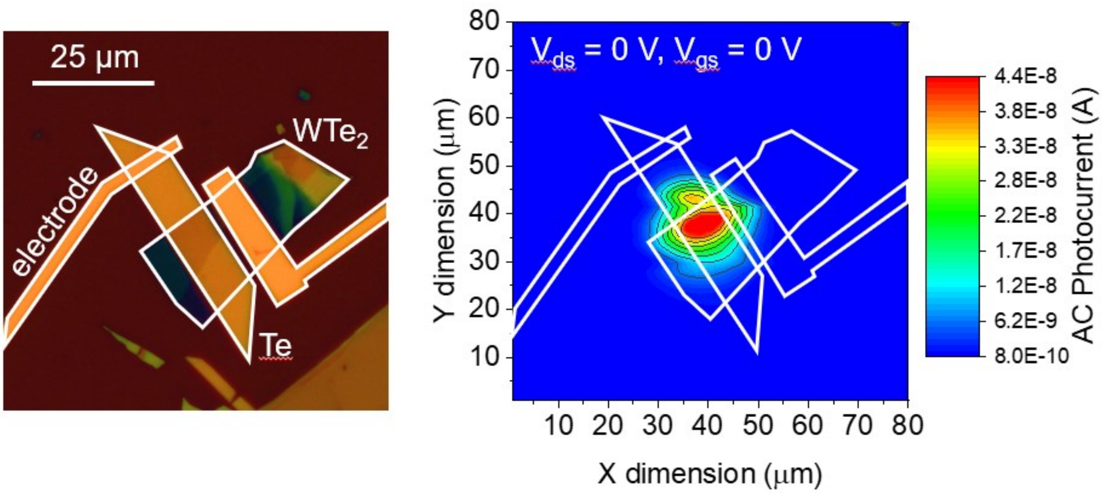

Figure S10. (a) optical image (b) photocurrent mapping image of 2D Te-WTe_2 heterostructure under an illumination using 1064 nm laser.

11. Response time of the device

We carried out the response test of our device. The device was at V_{ds} = 10 mV and V_{gs} = 0 V. Pulse laser with the power of 3 μW shined the device and concurrently, the generated photocurrent was registered. To manifest the photothermoelectric behavior, we tested our devices with a few different wavelengths, 450 nm, 811 nm, and 1064 nm. The light pulses have a width of 10 μs and 50% of duty ratio, as shown below. The output signal increases with the wavelength. A much higher photocurrent is generated with 1064 nm comparing to that of 450 nm. The results indicate that our optical detector is more sensitive at IR range rather than visible range. The response time of approximately 1.2 μsec was acquired with 1064 nm. The comparative test with different wavelengths is present in **Figure S11d**.

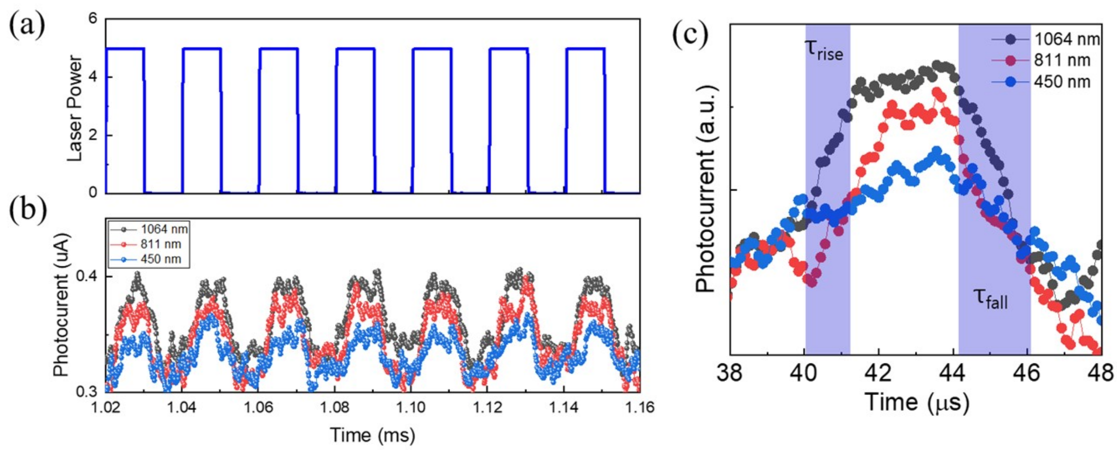

(d)

Wavelength (λ)	450 nm	811 nm	1064nm
Rise time (μsec)	3.6	1.6	1.2
Fall time (μsec)	3.2	2.0	1.9

Figure S11. Time domain plot (a) laser power pulses (b) corresponding photocurrent pulses with different wavelengths. (c) a single shot of photocurrent (d) response timetable.

12. Photocurrent distribution and source-drain bias

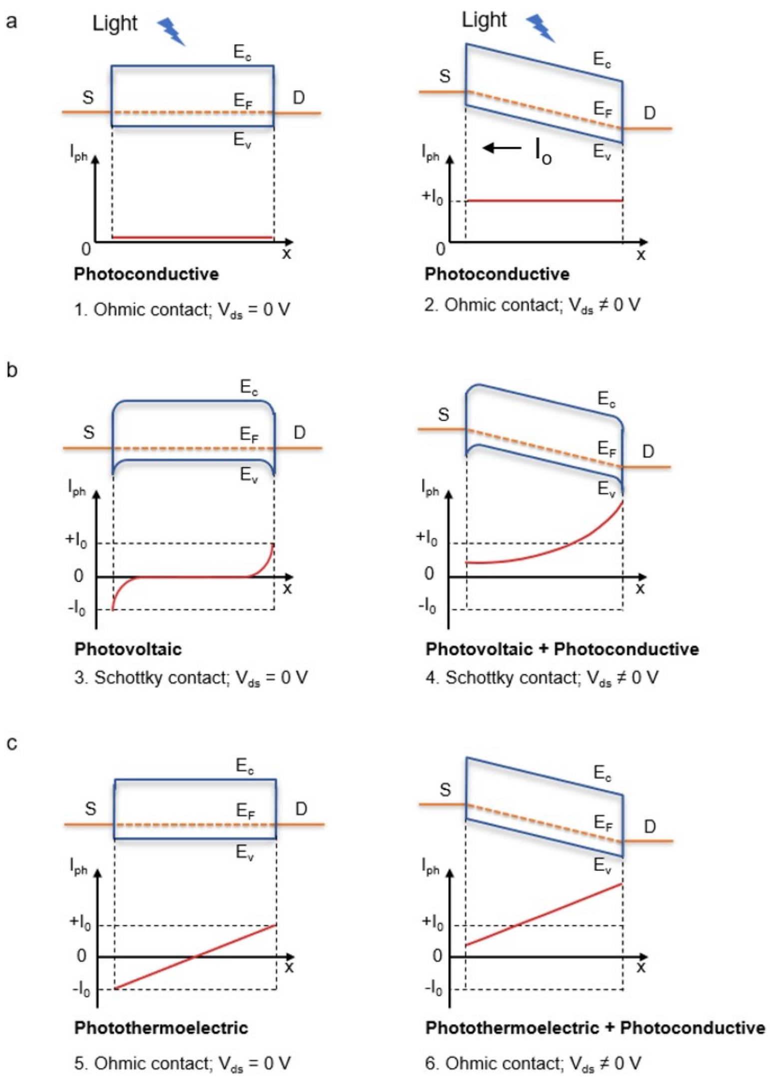

Figure S12. The line profile of the photocurrent (a) photoconductive, (b) photovoltaic, and (c) photothermoelectric with and without V_{ds}.

In Figure S12, a semiconductor device with source (S) and drain (D) electrodes was exposed to the incident light. The solid red line in the graph represents the photocurrent along the channel. As shown in Figure S12a, the device formed an ohmic contact with the metal electrodes, and the current flowing into the source current was positive. In the absence of V_{ds}, the photocurrent was very low. The small photoconductivity (PC) is attributed to the diffusion of the photoexcited carriers. When V_{ds} was applied, a significant increase in PC occurred because the electron-hole pairs were effectively separated. The current remained constant along the channel. When a semiconductor forms Schottky junctions at the metal electrode, the local built-in potential near the metal–semiconductor junction contributes to the photovoltaic (PV) current. Because the channel was not under V_{ds}, the PV current generation was evident only near the junction, and the current flowed in the opposite direction at the end. If we apply V_{ds} to the channel, the PC levels up the PV current. Along the channel, the current (PC + PV) is positive, and its intensity varies depending on the position because of V_{ds}. A PTE is generated along the channel when the incident laser heats the channel. The PTE is at its maximum at the channel end and decreases to zero at the center of the channel. Under V_{ds}, the current (PC + PTE) is upshifted by PC. Different from Figure S11b, the PC+PTE current was linearly dispersed along the channel.

13. Photocurrent map from WTe_2-2D Te at V_{ds} = 2 V as a function of V_{gs}

The modulations of the photocurrent intensity, direction, and position in the WTe_2-2D Te heterojunction were registered as a function of V_{gs} using our system. In Figure S13, the backgate bias was swept from V_{gs} = -40 V to V_{gs} = 40 V at V_{ds} = 2 V. The photocurrent was mostly generated in the 2D Te channel near the junction with WTe_2 at low V_{gs}, signifying the dominant photovoltaic effect. When V_{gs} increases, the photovoltaic effect decreases, whereas the photothermoelectric effect is enhanced.

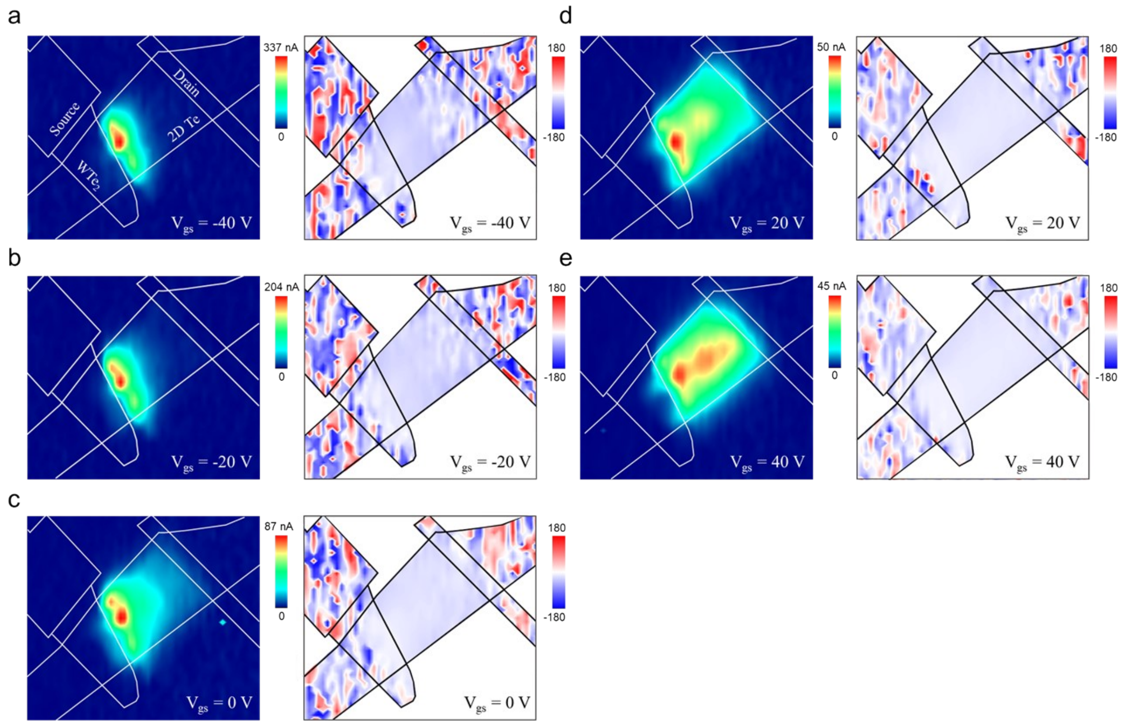

Figure S13. Magnitude-, phase-, and position-resolved photocurrent mapping images of WTe_2-2D Te as a function of V_{gs} at V_{ds} = 2 V. The input optical power is 5 μW. (a) V_{gs} = -40 V, (b) V_{gs} = -20 V, (c) V_{gs} = 0 V, (d) V_{gs} = 20 V, and (e) V_{gs} = 40 V.

14. Photocurrent map from WTe_2-2D Te at V_{ds} = –2 V as a function of V_{gs}

The distribution, intensity, and direction of the photocurrent from the WTe_2-2D Te heterostructure were obtained by varying V_{gs} at V_{ds} = –2 V. The typical photocurrent on the 2D Te channel near the drain electrode increased with V_{gs}, exhibiting the typical photothermoelectric behavior of 2D Te.

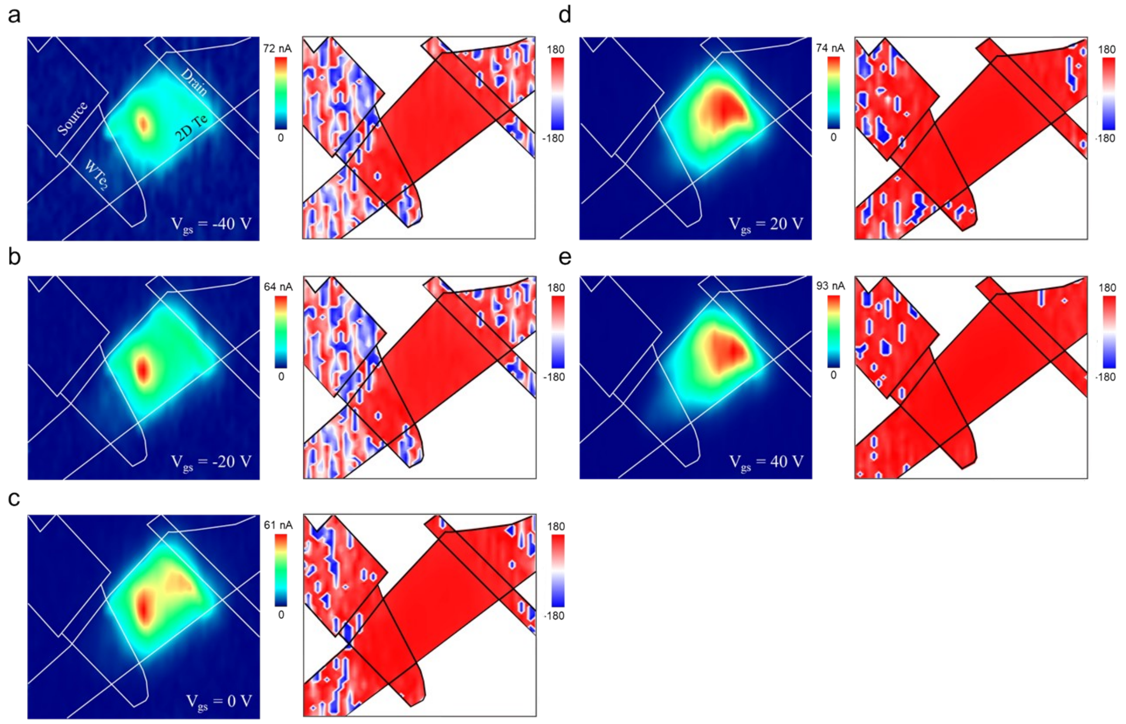

Figure S14. Magnitude-, phase-, and position-resolved photocurrent mapping images of ReS_2-2D Te as a function of V_{gs} at V_{ds} = –2 V. The input optical power is 5 μW. (a) V_{gs} = -40 V, (b) V_{gs} = -20 V, (c) V_{gs} = 0 V, (d) V_{gs} = 20 V, and (e) V_{gs} = 40 V.

15. Bias controlled photocurrent mechanism in WTe_2-2D Te heterostructure

	V_{gs} / V_{ds}	Increasing V_{gs}
WTe_2-2D Te Semimetal-Semiconductor junction	-2 V	Increasing PTE on 2D Te
	0 V	Increasing PTE on WTe_2-2D Te
	2 V	Decreasing PV on 2D Te

Table 1. Photocurrent mechanism in WTe_2-2D Te heterostructure at different bias conditions.

References:

[1] Verma, S., Yadav, R., Pandey, A., Kaur, M. and Husale, S., 2023. Investigating active area dependent high performing photoresponse through thin films of Weyl Semimetal WTe_2. *Scientific Reports*, *13*(1), p.197.

[2] Bhargavi, K.S., Patil, S. and Kubakaddi, S.S., 2015. Acoustic phonon assisted free-carrier optical absorption in an n-type monolayer MoS_2 and other transition-metal dichalcogenides. *Journal of Applied Physics*, *118*(4).